JOURNAL OF GEOPHYSICAL RESEARCH, VOL. 97, NO. C1, PAGES 611–626, JANUARY 15, 1992

Hydrographic Patterns and Vertical Mixing in the Equatorial Pacific Along 150°W

MARY-ELENA CARR,[1,2] NEIL S. OAKEY,[3] BURTON JONES,[4] AND MARLON R. LEWIS[5]

The WEC88 cruise sampled along a meridional transect from 15°N to 15°S along 150°W from February 17 to March 18, 1988, with a 6-day time series at the equator. The large-scale hydrographic patterns were typical for boreal spring. Equatorial maxima in dissipation of turbulent kinetic energy ϵ, and of thermal variance χ, were found between 2°N and 2°S for the top 60 m. The equatorial time series coincided with a shift from southward to northward velocity, which returned the zonal current system to the equator. This led to a decrease in temperature, and increases in salinity, nutrient, and chlorophyll concentrations in the surface layer. Vertical diffusivity as well as ϵ and χ increased with the observed intensification of the Equatorial Undercurrent. Maximum values of ϵ and χ were observed at around 55 m, and the temporal trends occurred first at depth. Turbulent heat flux out of the mixed layer was the same order of magnitude as the penetrative irradiance at that depth. Maximum vertical heat flux occurred at depth in response to large diffusivity coefficients. The Richardson number was useful in predicting the regions of enhanced mixing in the meridional transect. However, for the equatorial time series, where the *Ri* was less than 0.45, intensity of dissipation was not proportional to Richardson number.

1. INTRODUCTION

The large-scale patterns of current velocity and of scalars such as temperature, nutrient concentrations, and biological productivity in the equatorial Pacific are determined by the zonal current system. The zonal flow is driven by the easterly winds; at the surface (and at depth poleward of 0°) the South Equatorial Current (SEC) flows to the west. At depth the transport is eastward in the form of the Equatorial Undercurrent (EUC) at 0° and the North Equatorial Counter Current (NECC) to the north. Associated with the intense zonal flow is a weaker meridional pattern which is poleward on the mean above the EUC (Ekman divergence) and equatorward at depth. An upwelling velocity, estimated as $1\text{-}3\times10^{-5}$ m s^{-1} [*Bryden and Brady*, 1985; *Brady and Bryden*, 1987; *Halpern and Freitag*, 1987; *Halpern et al.*, 1989] is associated with the Ekman divergence above the EUC core. The upwelling of cold, nutrient-rich water which warms because of solar heating and becomes nutrient depleted due to biological uptake as it flows poleward explains the characteristic temperature minimum and nutrient maximum found at the equator.

The seasonal cycle of the equatorial region [*Wyrtki*, 1974; *Wyrtki*, 1975*b*; *McPhaden and Taft*, 1988; *Wilson and Leetmaa*, 1988] is characterized by small variations in surface temperature (compared with higher latitudes) and significant changes in the strength and position of the equatorial current system. During boreal spring the EUC shoals and attains maximum intensity [*McPhaden and Taft*, 1988; *Wilson and Leetmaa*, 1988]. The strongest westward winds are observed in autumn and are accompanied by maximum westward flow. The seasonal cycle is subject to both lower frequency variability, e.g., on an interannual scale, the El Niño-Southern Oscillation (ENSO) [*Wyrtki*, 1975*a*; *Philander*, 1989] and higher frequency oscillations, e.g., the 4-day "pulses" corresponding to the passage of equatorially trapped Kelvin waves [*Wunsch and Gill*, 1976; *Chereskin et al.*, 1986].

The interaction between large- and small-scale physics is unique in the equatorial region and is of great interest both in prediction of global climate and in determining the role of equatorial processes in the global CO_2 cycle. The EUC, although subject to the above variability, provides a steady large vertical shear. This mean shear makes the region above the EUC core an "ocean-scale laboratory for shear-driven turbulence" [*Peters and Gregg*, 1988]. Turbulent mixing of heat, momentum, and nutrients have been put forward as playing a significant role in equatorial dynamics. For example, cold or warm sea-surface temperature (SST) anomalies in the equatorial Pacific, which result from variability in the mean flow and its fluctuations, modify the air-sea exchange of heat and moisture, and have been linked to displaced atmospheric circulation patterns over the American continent [*Bjerknes*, 1969; *Wyrtki*, 1975*a*; *Horel and Wallace*, 1981; *Eriksen*, 1985; *Trenberth et al.*, 1988]. Turbulent mixing and upwelling enrich the surface ocean with nutrients and enhance "new" production [*Chavez and Barber*, 1987]. Likewise, CO_2 rich water is brought to the surface, where it outgasses to the atmosphere.

The goal of the WEC88 cruise was to study the interaction of hydrographic patterns and physical forcing on large- and small- scales and to quantify their role in equatorial biogeochemical processes. The WEC88 cruise sampled along a meridional transect from 15°N to 15°S along 150°W from February 17 to March 18, 1988. Here we wish to provide a characterization of the large-scale hydrographic conditions observed during the cruise, as well as to address the small-scale physical measurements taken. Our goal is to provide a physical context for the other papers in this issue, of a more biological nature, as well as to interpret the vertical mix-

[1]Department of Oceanography, Dalhousie University, Halifax, Nova Scotia, Canada.
[2]Now at College of Oceanography, Oregon State University, Corvallis, Oregon.
[3]Department of Fisheries and Oceans, Bedford Institute of Oceanography, Dartmouth, Nova Scotia, Canada.
[4]Institute of Marine Sciences, University of Southern California, Los Angeles, California.
[5]Department of Oceanography, Dalhousie University, Halifax, Nova Scotia, Canada.

Paper number 91JC02479.
0148-0227/92/91JC-02479$05.00

ing patterns in terms of the large-scale hydrography. The large-scale conditions, typical for northern spring, led to different equatorial mixing patterns from observations made in November 1984 during Tropic Heat [*Peters and Gregg*, 1988; *Moum et al.*, 1989]. The sampling period coincided with the end of the warming episode of the 1986-1987 El Niño and the start of a cooling event, which would culminate in May with SST anomaly patterns that have been linked to the extensive drought conditions observed in summer of 1988 in North America [*Janowiak*, 1988; *Trenberth et al.*, 1988]. Cold sea-surface temperatures during our study period led to low values of surface heat losses to the atmosphere and were accompanied by high values of turbulent heat flux at depth.

A discussion of experimental details and data analysis techniques used is given in section 2. In section 3 we address the results of the meridional transect: meteorological conditions, hydrographic patterns, and the small-scale physics. The equatorial time series is discussed in section 4, also by examining the meteorological conditions, large-scale hydrography, and microstructure measurements. The parameterization of vertical mixing using the Richardson number is addressed in section 5, followed by a discussion in section 6 and conclusions in section 7.

2. Experimental Details and Data Analysis

The R/V *Wecoma* surveyed from 15°N to 15°S along 150°W (cruise WEC88) in February-March 1988. The sampling scheme is summarized in Figure 1. Conductivity, temperature, and depth (CTD) measurements, using a Neil Brown system, of finescale temperature and salinity of the top 400 m were made in hydrographic drops every 2°30′ between 15° and 5° (S and N) and then at 2°, 1° and 0° every 6 hours when on site.

Currents to a depth of approximately 150 m were measured with an RDI Acoustic Doppler Current Profiler

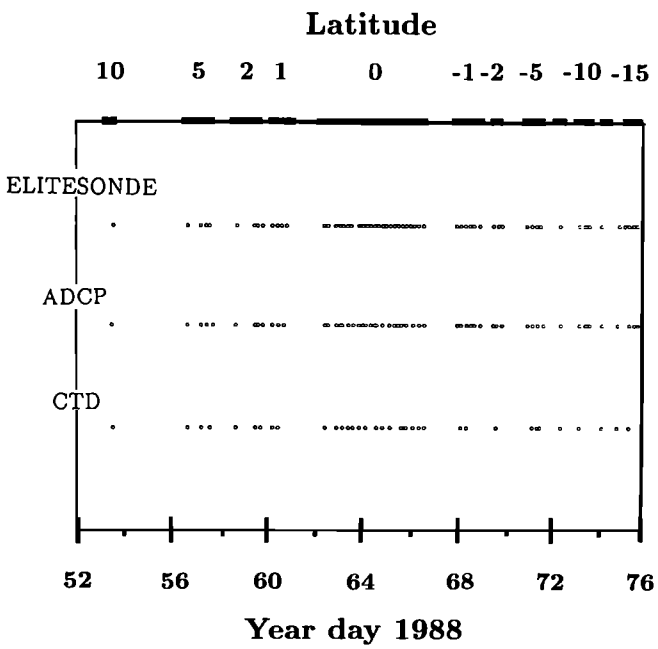

Fig. 1. Sampling scheme. The horizontal axes are time (lower) and latitude (upper). The circles indicate stations from either hydrographic casts (CTD and nutrients), ELITESONDE, or ADCP. Negative latitudes are south.

(ADCP). The Doppler-shifted frequency of the reflected signal was used to calculate the water motion relative to the ship in 8 m bins. Absolute velocities can be obtained using precise navigational records or an independent estimate of current to remove the ship motion. Lacking both of these, an arbitrary reference depth was chosen and subtracted from all depth bins. The chosen depth bin was centered at 14 m, based on the results of *Bryden and Brady* [1985], which indicate that for the mean velocity at the equator, the cross-over between the westward flowing surface current and the eastward undercurrent occurs at around 15 m. This choice may be suitable for the zonal flow at the equator but may not be the best choice for the rest of the transect. However, for the purposes of this paper, a qualitative scenario of general flow patterns is sufficient. The ADCP data are used here to estimate shear, which is independent of the reference depth chosen. Two minute velocity measurements were averaged to provide hourly estimates that made up the basic dataset. The error associated with the relative velocities is estimated to be less than 0.05 m s^{-1}.

Microstructure measurements of temperature and shear were made with ELITESONDE, a 1.75 m free-falling vertical profiler, similar to EPSONDE [*Oakey*, 1988]. The instrument measures temperature microstructure with a glass-bead thermistor and two components of horizontal velocity shear using probes similar to those described by *Osborn and Crawford* [1980]. Three to six vertical profiles were made at each station. One to 24 stations were occupied at the following latitudes: 10°N, 5°N, 2°N, 1°N, 0°, 1°S, 2°S, 5°S, 7.5°S, 10°S, 12.5°S and 15°S. A time series of 4.5 days, with stations every 4 hours was carried out at the equator.

The concentrations of nitrate, nitrite, and silicate were measured using standard automated techniques [*Whitledge et al.*, 1981] on water samples collected during the hydrographic casts using 5L Niskin bottles on a rosette. The uncertainty of the nitrate and silicate determination is less than 5%. Chlorophyll concentrations, obtained by filtering water samples on Whatman GF/F filters and extracting in 90% acetone, were determined with a Turner Designs 10-005R fluorometer; again, standard deviations of replicate determinations are less than 5% of the mean value.

The buoyancy frequency (N) was determined by doing a 13-m least squares linear fit of density to depth. The error in N^2 is estimated to be less than 10% for large values ($N^2 \simeq 10^{-4}$ s^{-2}), while small values ($N^2 \simeq 10^{-6} s^{-2}$) are within a factor of 2.

Shear was calculated by first differencing the relative velocities (ADCP) measured below 20-m depth from adjacent 8-m bins and was then interpolated to 10-m depth intervals. The uncertainty associated with this method is twofold. Due to the averaging procedure inherent to the ADCP system, the velocities obtained for each depth bin are the result of triangular filtering of the Doppler shifted signals, leading to an underestimation of shear. Shear values are underestimated at all scales but particularly so if shear varies at scales close to the bin size [*Toole et al.*, 1987]. To assess the implications of this averaging, comparison was made between shear calculated over 8-, 16-, and 32-m depth intervals. Similar values were obtained for each case. The only difference was found at the equator: a slight overestimation of shear when calculated at the smaller scale at one depth interval in each profile (typically close to the EUC core). It seems that there was high wavenumber variability which was aver-

aged out on larger scales. In the case of *Toole et al.* [1987], where larger depth intervals yielded higher shear estimates, the low-wavenumber variability was not resolvable on the smaller scale. Because it is not possible to estimate shear at smaller intervals than the bin size, our measurement is necessarily less than or equal to the actual shear. This implies that the estimates of Richardson number and of K_m are an upper bound. The error associated with the shear values was estimated as in *Toole et al.* [1987] by calculating the variance of the hourly averages. It is found to be less than 10% of the measured shear for both components.

The Richardson number was estimated from the CTD and ADCP data using

$$Ri = \frac{-g/\rho\ \partial\rho/\partial z}{(\partial u/\partial z)^2 + (\partial v/\partial z)^2} \tag{1}$$

where g is gravity, ρ is the density of water, and u and v the north and east velocity components. The error in Richardson number is estimated to be approximately 20% for large N^2 and a factor of 2 for small N^2. In general, the largest shears (observed above the EUC) coincide with large values of N^2.

Microstructure data analysis is similar to that of *Oakey* [1985]. The shear power spectra (having corrected for sensor and instrument electronic response) were examined to determine the spectral minimum (at the gap between signal and noise), which was used as the cutoff point for integration. A variety of editing criteria (including comparison to a theoretical universal curve) were used to reject data contaminated by spurious instrument noise.

The rate of dissipation of turbulent kinetic energy, ϵ, is calculated assuming isotropic turbulence using

$$\epsilon = \frac{15}{2}\,\nu\,\overline{\left(\frac{\partial u'}{\partial z}\right)^2} \qquad [\mathrm{W\ kg^{-1}}] \tag{2}$$

where the prime denotes a fluctuating quantity, as opposed to the mean (Reynolds decomposition), and is measured with ELITESONDE, and ν is the kinematic viscosity ($\nu = 1.3 \times 10^{-6}$ m^2 s^{-1}).

In the case of temperature variance, the frequency response of the glass-bead thermistor could not resolve the spectral gap for high dissipation rates. Temperature variance was determined to a fixed frequency (or wavenumber), and the "lost variance" was estimated by determining what portion of a theoretical Batchelor curve this wavenumber represented in comparison to the Batchelor cut-off wavenumber, $k_B = (\epsilon/\nu D^2)^{1/4}$ (where D is the molecular diffusivity, $D = 1.4 \times 10^{-7}$ m^2 s^{-1}) representing 100%. The fraction of thermal variance that was resolved by our thermistor varied from 99%, in regions of low dissipation, to 45% in the high shear zone at the equator (see Figure 15*b*).

The rate of dissipation of thermal variance, χ, is given by

$$\chi = 6\,D\,\overline{\left(\frac{\partial T'}{\partial z}\right)^2} \qquad [\mathrm{°C^2\ s^{-1}}] \tag{3}$$

where T' is the microscale temperature measured by ELITESONDE.

Three coefficients of vertical eddy diffusivity were estimated using microstructure and large-scale measurements. The vertical eddy coefficient for heat, K_T, is estimated using the Osborn-Cox model [*Osborn and Cox*, 1972]:

$$K_T = 3\,D\,Cox \qquad [\mathrm{m^2\ s^{-1}}] \tag{4}$$

where

$$Cox = \frac{\overline{(\partial T'/\partial z)^2}}{(\partial \overline{T}/\partial z)^2} \tag{5}$$

where T' is the microscale temperature fluctuation and $\partial\overline{T}/\partial z$ is the mean temperature gradient in a given depth interval.

The turbulent heat flux, J_q, was calculated using the diffusivity for heat according to

$$J_q = -\rho\,C_p\,K_T\,\frac{\partial \overline{T}}{\partial z} \qquad [\mathrm{W\ m^{-2}}] \tag{6}$$

where C_p is the specific heat of water ($C_p = 4.129 \times 10^3$ J (kg°C)$^{-1}$).

The vertical eddy diffusivity for mass, K_ρ, is calculated using the *Osborn* [1980] model

$$K_\rho = \frac{R_f}{1 - R_f}\,\frac{\epsilon}{N^2} \qquad [\mathrm{m^2\ s^{-1}}] \tag{7}$$

where

$$\frac{R_f}{1 - R_f} = \Gamma \tag{8}$$

and R_f is the flux Richardson number and Γ is called the mixing efficiency. Values for Γ have been proposed on theoretical grounds, based on a critical value for R_f [*Osborn*, 1980], as well as using actual measurements of shear and thermal variance, and assuming that the coefficients for heat and mass are the same [*Oakey*, 1985]. Both approaches lead to an approximate value of 0.25 for Γ.

The dissipation method [*Gregg et al.*, 1985] is used to obtain a value for the diffusivity coefficient for momentum, K_m,

$$K_m = \frac{\epsilon}{U_z^2} \qquad [\mathrm{m^2\ s^{-1}}] \tag{9}$$

where

$$U_z^2 = \left(\frac{\partial u}{\partial z}\right)^2 + \left(\frac{\partial v}{\partial z}\right)^2 \tag{10}$$

This method is only applicable where the major source of turbulent mixing is a steady mean shear and therefore is not appropriate for most of the open ocean, where turbulence is usually either surface-driven or the result of intermittent shear due to internal waves. Here it is used only at the equator.

The microstructure data of the first 10 m are discarded because of noise from wave action and the ship. Mean values for microscale shear and temperature variance are found for each "segment", a 4-s interval (corresponding to 4–6 m depth). The parameters for each segment were interpolated to produce values for 10-m depth intervals. For the equatorial time series the 95% confidence intervals for the mean value at each station were calculated assuming a lognormal distribution and using the method outlined in *Baker and Gibson* [1987]. For the meridional transect, the stations at each latitude were averaged to produce a mean value. The 95% confidence limits of this mean were calculated using the bootstrap method [*Efron and Gong*, 1983] with 500 samplings of the observed residuals. The confidence intervals were thus found at each latitude by subsampling the population of residuals the same number of times as stations at that latitude.

Surface heat fluxes were calculated with standard bulk

formulae [*Gill*, 1982]. Incoming irradiance was taken to be twice the value of the visible radiation (400–700 nm) [*Siegel and Dickey*, 1987] measured on the ships deck. Humidity was estimated using wet and dry bulb temperatures. Wind speed and direction were measured with the ship anemometer at 20 m every 10 min. The 10-min measurements were averaged to obtain hourly values. They were then corrected to 10 m with the logarithmic wind profile and the air-sea temperature difference using a program (B. Toulany and F. Dobson, personal communication, 1991) based on the procedures outlined by *Smith* [1988]. The surface buoyancy flux, J_b was estimated using:

$$J_b = \frac{g\,\alpha}{\rho\,C_p}\,(Q_+ + Q_-) \qquad [\mathrm{W\ kg^{-1}}] \qquad (11)$$

where Q_+ is the sum of latent, sensible and long-wave flux (i.e., the convective case), Q_- is the incoming short-wave flux, and α is the thermal expansion coefficient for seawater ($\alpha = 3 \times 10^{-4}\ ^\circ\mathrm{C}^{-1}$). To express the variability along the meridional transect, only the positive buoyancy flux was estimated because the incoming solar irradiance was essentially the same at all latitudes. The total surface heat flux (losses plus the incoming short-wave flux during the day) was used to calculate J_b for the equatorial time series.

3. Meridional Transect

It took 30 days to complete the 30° meridional transect, a period which is long compared to some of the most energetic phenomena controlling equatorial dynamics. "Slow" variability at a given site, e.g., associated with the 20- and 4-day waves [*Chereskin et al.*, 1986] cannot be resolved adequately by a cruise spanning 30° of latitude. Another problem is the aliasing introduced by insufficient sampling of the diurnal cycle. *Peters et al.* [1989] found that for a transect from 3°N to 3°S the diurnal variability was two decades, while the spatial variability was a factor of 3. In our 30° transect, although there were latitudes for which only day stations were taken (10°N, 7.5°S, and 12.5°S) and others that had predominantly night stations, for example, 2°S (1 day and 3 night stations) and 15°S (3 night and 2 day stations), all others had 2 day and 2 night stations (the equatorial time series had 14 day and 10 night stations). Thus we can consider that we have approximated the meridional structure by sampling the diurnal cycle at most latitudes.

Meteorological Conditions

The observed values of wind speed, surface heat loss (sum of latent, sensible, and long-wave), and convective buoyancy flux were averaged at each latitude (Figure 2). The most conspicuous aspect of both SST and air temperature (Figure 2*a*) along the cruise track is the equatorial minimum, increasing to maxima at 5°N and 10°S. The average air temperature was consistently greater than the SST. The largest wind speed (Figure 2*b*) was observed at 10°N, and for the rest of the transect, wind speeds were less than 7 m s^{-1}. The surface heat loss (Figure 2*c*), resulting from the sum of sensible, latent, and long-wave fluxes, reflects the pattern of wind speed and of air-sea temperature difference. We observe the largest heat loss at 10°N, where the difference is minimum and wind speed is largest. The lowest values occur where the air-sea temperature difference is greatest (0°, 2°N, 10°S). The pattern of J_{b+} (Figure 2*d*), estimated from the heat loss, is the same. The buoyancy flux and the wind stress are the major surface forcing terms for turbulent mixing.

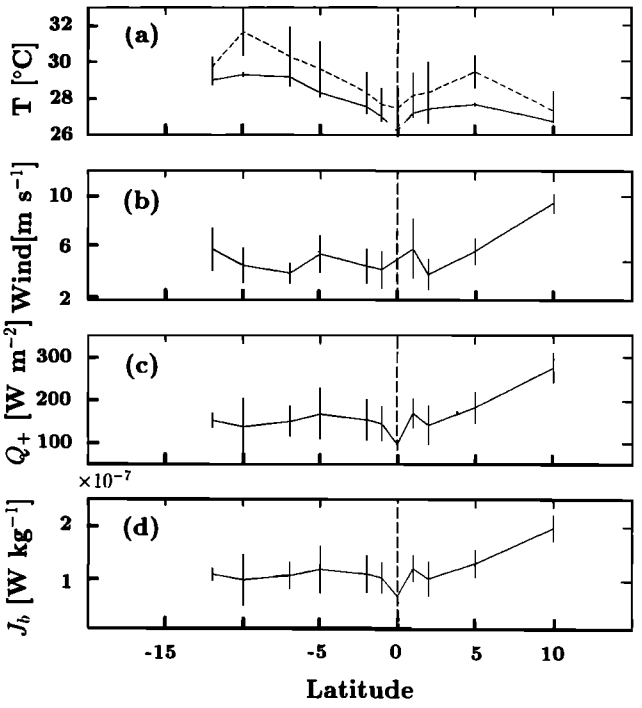

Fig. 2. Meteorological conditions along the meridional transect. (*a*) Air (dashed line) and sea surface temperature (solid line), (*b*) wind speed, (*c*) surface heat loss, calculated as the sum of the sensible, latent, and long wave flux terms, and (*d*) surface buoyancy flux. Negative latitudes are south.

Hydrographic Patterns

The contour plot of temperature along the meridional transect (Figure 3*a*) is similar to the ridge-trough system described by *Wyrtki and Kilonsky* [1984] as well as the model output of *Bryden and Brady* [1985]. Two pools of warm water are separated by the cold water of the equatorial divergence; this trend is reflected in the air temperature as well (Figure 2*a*). The 25° to 11°C isotherms dome at around 10°N, deepen at 5°N to shoal again at the equator, an effect of the upwelling associated with the EUC. They deepen again beyond 2°S. The warmest water (>29°C) is found in the top 75 m south of 7.5°S. The salinity structure (Figure 3*b*) is markedly asymmetric around the equator, with fresher water to the north. A front, marked by the 35 practical salinity unit (psu) isoline, intersects the surface at 0° and extends to about 330 m at 15°S. This clear polarity north-south/ high-low salinity is attributed to the excess precipitation over evaporation in the Intertropical Convergence Zone (5-10°N) [*Bryden and Brady*, 1985]. A subsurface salinity maximum (>36 psu) is found south of 5°S between 100 and 200 m depth. This high-salinity water is presumably formed in the subtropical gyre, where evaporation is very high.

The clearest feature of the relative eastward velocity (Figure 4*a*) is the presence of the EUC. Maximum velocity relative to the 15-m depth bin is found at the equator at a depth of 78 m. This is typical for spring [*McPhaden and Taft*, 1988; *Wilson and Leetmaa*, 1988]. The NECC, found north of 8°N and below 50 m, also flows to the east. South of 5°N the predominant flow is the westward SEC, which at-

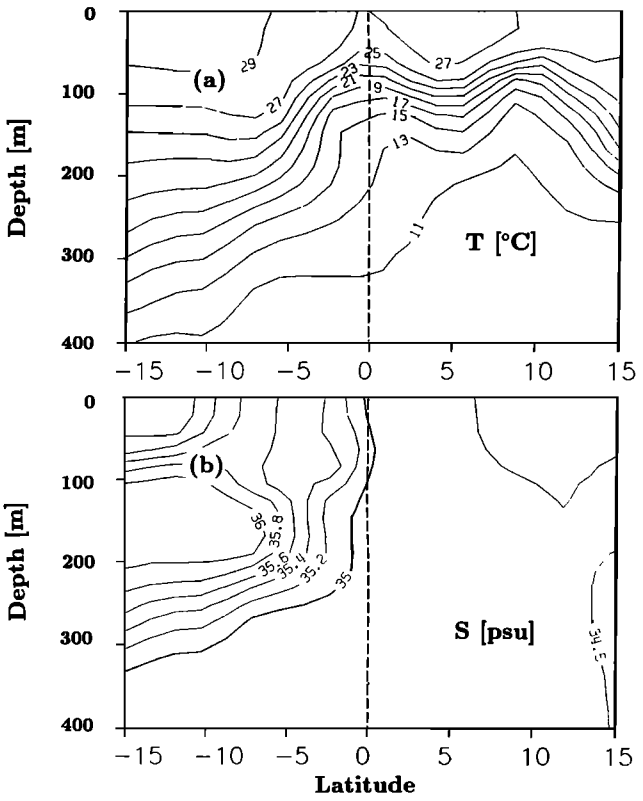

Fig. 3. Contour plots of (*a*) temperature, and (*b*) salinity along the meridional transect. Negative latitudes are south.

tains maximum relative values at 50 m and deeper, between 8°S and 15°S. The high velocities associated with the EUC extend to 2°S and to 1°N (1 m s^{-1} isoline).

The relative meridional velocity (Figure 4*b*) is of small magnitude (O(0.1 m s^{-1})). Above the core of the EUC (20–75 m), the meridional flow diverges (Ekman divergence of the upwelled water), while at and below the core (75–150 m) there is a convergence (Figure 4*c*). The southward velocity is stronger than the northward velocity in both the divergence and the deeper convergence (Figure 4*b*). The divergence and convergence are centered slightly to the north of the equator. This is the classical circulation pattern, which we would expect to be obscured by high-frequency variability within a single transect. A possible explanation for our observations is that, as will be seen later, we sampled the shift between southward and northward flow at 0°. This sign change in flow direction during our sampling period may have enabled the visualization of the meridional cell by averaging out the short-term variability.

The concentrations of nitrate, silicate, and nitrite are shown in Figure 5, and the chlorophyll concentration in Figure 6. The meridional patterns of NO_3 and SiO_4, the chemical substrates for photosynthetic production, follow that of temperature, with low surface values, a region of high concentration gradient (nutricline), and high concentrations at depth. In the equatorial region, the concentrations are comparable to those of the upper thermocline. The highest concentrations observed are found below the shallow nutricline from 6°N to 15°N, and the lowest are those of the mixed layer south of 5-10°S. In this region, the nutricline is found below the maximum temperature gradient. This is a consequence of the presence of low-nutrient, high-salinity subtropical water in the upper thermocline. Nitrite, a tracer of subtropical water [*Wyrtki and Kilonsky*, 1984] presents maxima up to 2 μmol L^{-1} along the thermocline south of the equator. Nitrite values are generally less than 0.5 μmol L^{-1} at and north of the equator. North of the equator the silicate concentration in the upper 100 m generally exceeds the nitrate concentration. The situation is reversed between the equator and 7.5°S. This may have consequences for the phytoplankton community type: in regions where silicate is less than nitrate, the balance is likely to shift more toward non diatom species or toward diatoms with relatively low silicon requirements. *Chavez* [1989] observed that on the equator between 90° and 150°W, most of the chlorophyll was con-

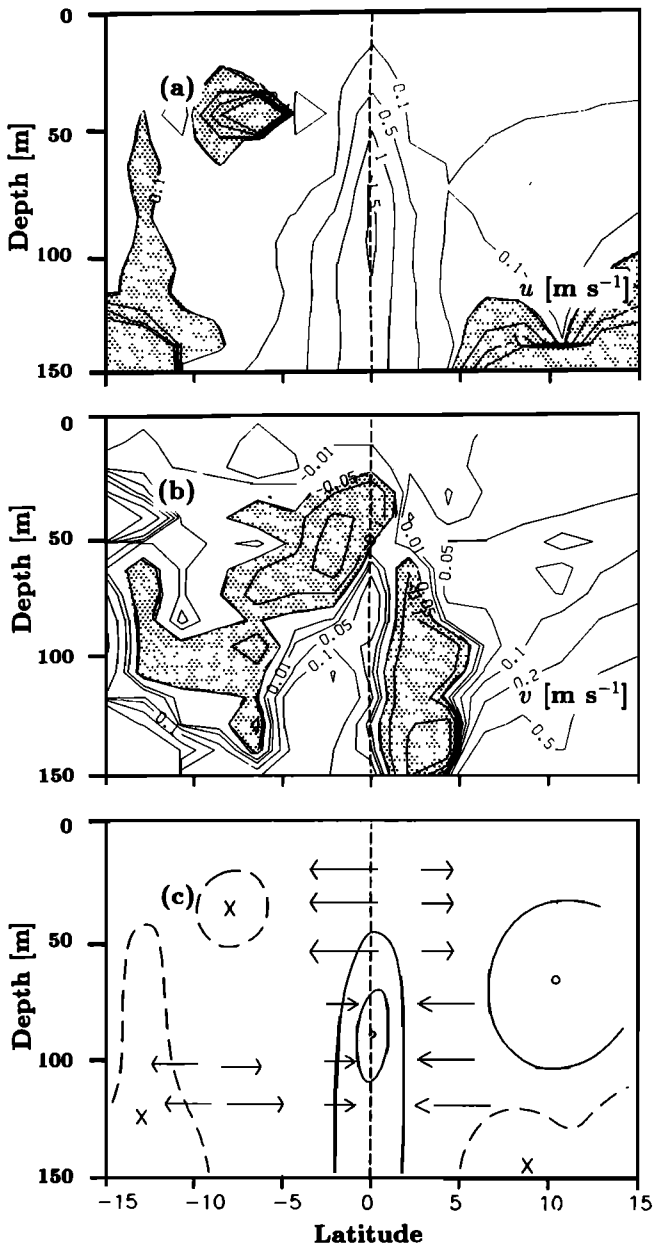

Fig. 4. Contour plots of (*a*) relative east-west velocity and (*b*) relative south-north velocity. The shaded areas are westward velocity in Figure 4*a* and southward velocity in Figure 4*b*. (*c*) Cartoon illustrating the flow pattern during the meridional transect; the contours represent east-west velocity (out of and into the page, respectively), and the arrows meridional flow. Negative latitudes are south.

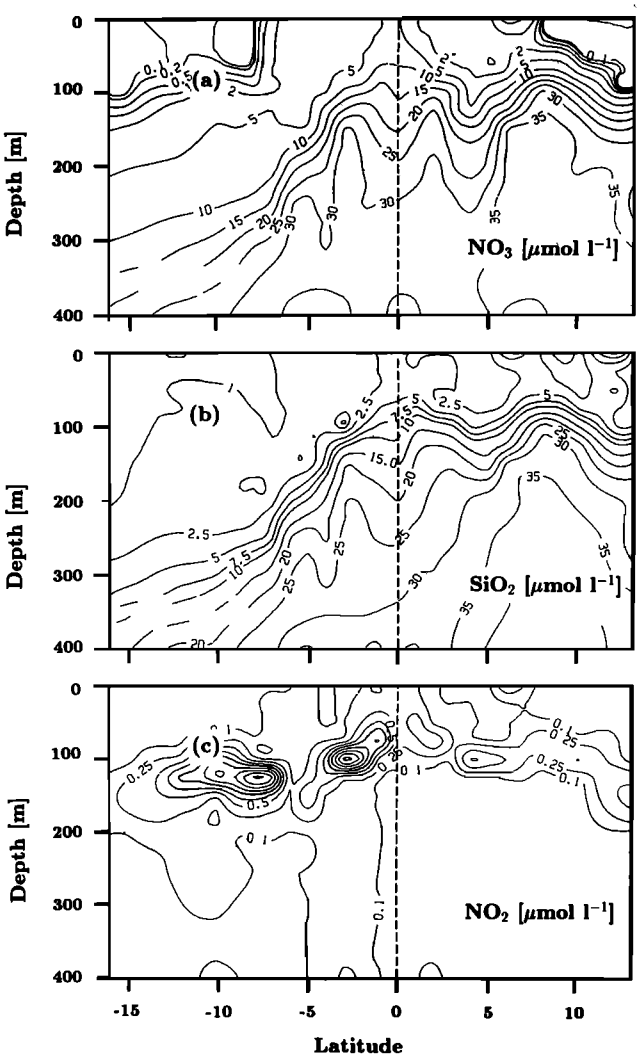

Fig. 5. Contour plots of concentration of (*a*) nitrate; (*b*) silicate, and (*c*) nitrite in the meridional transect. Negative latitudes are south.

tained in the size fraction smaller than 1 μm in diameter, i.e., the picoplankton. Likewise *Peña et al.* [1990] found that cells smaller than 10 μm made up 90% of the population at 135°W. This is consistent with the idea that large diatoms are much less important than in coastal upwelling, where nutrient concentrations are comparable. The chlorophyll concentration (Figure 6) presents the typical tropical structure with a deep chlorophyll maximum, ranging from 150 m at around 5°N to 60 m at the equator.

The meridional transects of stability, N^2, shear (U_z^2), and Ri are shown in Figure 7. There is a maximum in N^2 from 0° to 1°N between 10 and 30 m. For the 35–55 m depth intervals this peak becomes more pronounced and wider, extending latitudinally from 1°N to 1°S. The high values found close to 0° are related to the equatorial divergence, where the mixed layer is shallow and the thermocline is close to the surface as a result of upwelling. The low N^2 for the surface bin at 10°N may be related to the maximum in wind stress and buoyancy flux observed there (see Figure 2). The minima at 5°N and at 7.5°S coincide with the warm water pools found in these regions (Figure 3*a*).

In Figure 7*b* the meridional, zonal, and total shear squared are shown. The value of total shear squared is below 10^{-4} s^{-2} except for the equatorial region from 2°N to 2°S between 20 and 50 m; the 55 and 65 m depth bins reveal high shear values at 5°N as well. The high equatorial U_z^2 signal is a consequence of the EUC, as is revealed in the zonal component. South of 2–5°S the meridional component is predominant. Although the zonal component is largest around 0°, the meridional shear can be decisive in raising the total value.

The Richardson number (Ri) is obtained by merging the N^2 from the CTD and the shear data from the ADCP. The meridional pattern of Ri is shown in Figure 7*c*. It is through Ri that we can provide a link between the large-scale (CTD and ADCP) measurements and the small-scale microstructure measurements (ELITESONDE). The $Ri < 1/4$ threshold criterion for shear-flow instability [*Miles*, 1961] allows us to anticipate the regions where turbulent mixing is to be expected. Parameterizations of the mixing coefficient based on Ri have been proposed for use in models of equatorial dynamics [*Pacanowski and Philander*, 1981]. The Richardson number shows values <1/4 from 1°S to 1°N at 25 m; at 35 m between 2°S and 1°N and at 45 m from 1°S to 0°. Below 50 m there are no values below 1/4, although at the equator, Ri is approximately 1/4. Only between 2°S to 1°N are values of $Ri \leq 1/4$ found from 10 to 50 m. The equatorial minimum in Ri, in spite of large N^2, is a result of high shear at 0°. In addition to the EUC, strong variations in

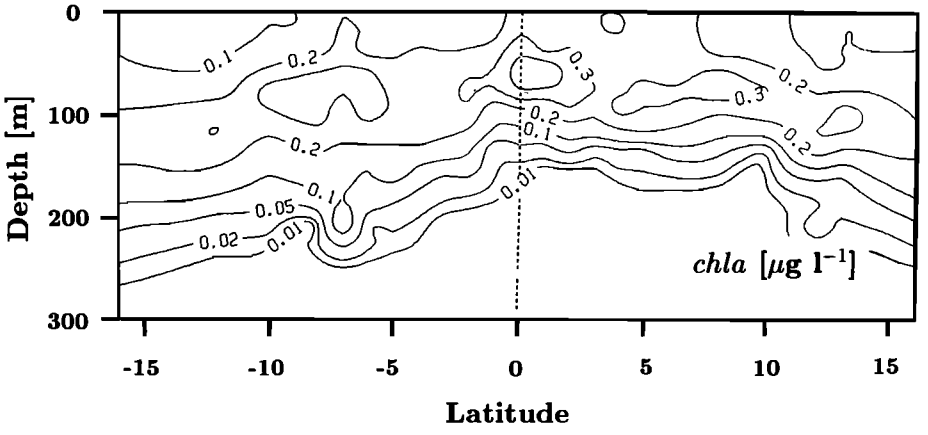

Fig. 6. Contour plot of chlorophyll concentration in the meridional transect. Negative latitudes are south.

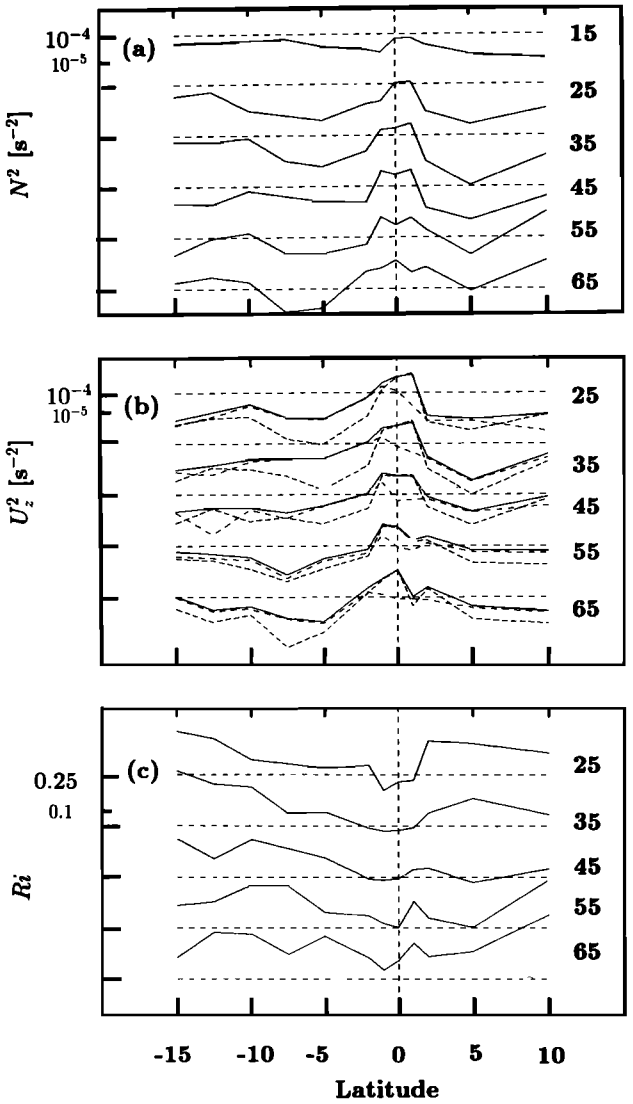

Fig. 7. The average (*a*) N^2, (*b*) U_z^2, and (*c*) *Ri* for each bin interval of the microstructure stations in the meridional transect. Negative latitudes are south. In Figure 7*b* the solid line is the total shear U_z^2, the dashed line is the zonal component u_z^2, and the dotted line is the meridional component v_z^2.

meridional velocity are also important [*Toole et al.*, 1987]. The southward displacement of the equatorial *Ri* minimum between 40 and 50 m is not related to the N^2 values, as similar high values are found at 1°N and 1°S. Likewise at that depth the EUC is symmetrical around 0°. The meridional component of shear (see Figures 7*b* and 4*b*) is responsible for the low *Ri* to the south; this is similar to observations made by *Toole et al.* [1987] for an equatorial time series.

Small-Scale Physics: Dissipation and Vertical Mixing

The meridional pattern of turbulent kinetic energy dissipation, ϵ, is seen in Figure 8*a*. Each line is the mean value observed at each latitude for the specified 10-m intervals centered at 15 m, 25 m, 35 m, 45 m, 55 m, and 65 m. The dotted lines are the 95% confidence limits for the calculated mean. At three latitudes (10°N, 7.5°S, and 12.5°S) there was only one station (2-6 vertical profiles). At these latitudes the confidence intervals are the same order of magnitude as the range of the residuals of the entire transect at that depth: from two to three decades. The highest individual values of ϵ observed are greater than 10^{-6} W kg^{-1} at the equator (see Figure 15*a*). The lowest values were observed south of 5°S. The observed meridional pattern is similar at all depths: a maximum in the equatorial region and minima at 2°N and 5°S. Poleward of the minima it either levels off or increases. Except for 10°N at 15 m, the mean is always less than 10^{-8} W kg^{-1} outside of the equatorial region. The southward bias of the equatorial maximum below 40 m reflects the observations of *Ri* (Figure 7*c*), and is a consequence of the larger shear south of the equator in the meridional divergence between 30 and 55 m (Figures 3*b* and 7*b*). The large surface values of ϵ at 10°N correspond to the largest observed values of buoyancy flux and wind stress (Figures 2*b*, 2*c*).

The equatorial peak is statistically significant within 95% confidence limits for 0° to 1°S between 40 and 70 m. The dissipation values north of 1°N are significantly distinct with

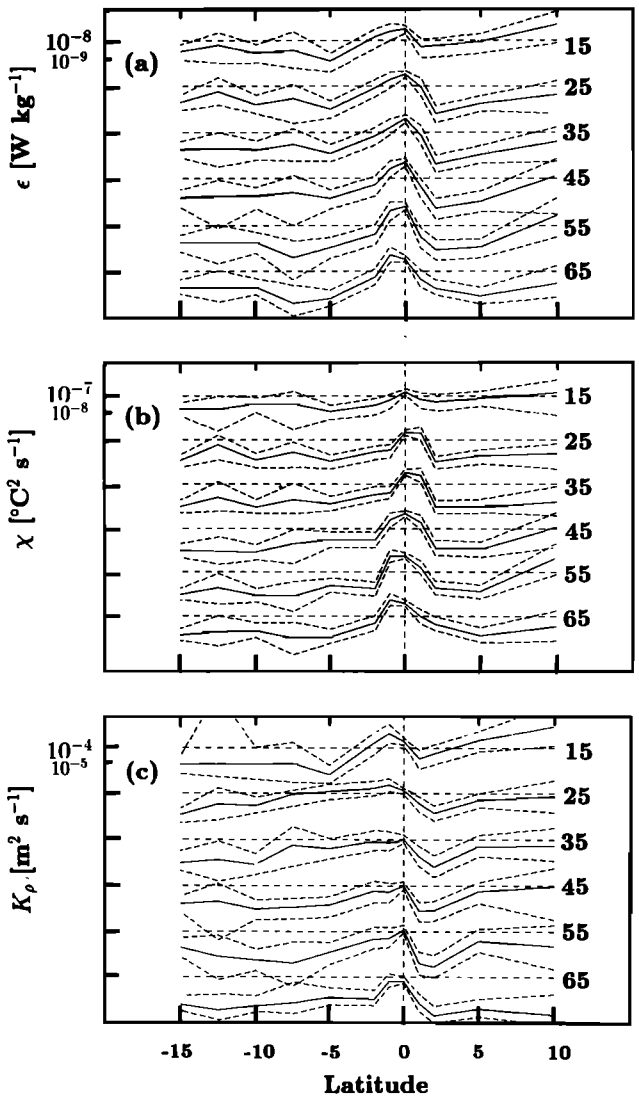

Fig. 8. (*a*) Turbulent kinetic energy dissipation ϵ, (*b*) dissipation of thermal variance χ and (*c*) the vertical eddy diffusivity K_ρ along the meridional transect. The solid line is the mean for each depth interval at that latitude, and the dashed lines are the 95% confidence intervals.

respect to the equatorial region at all depths. The uncertainty south of 5°S is large enough that we cannot positively identify an equatorial peak above 40 m. A detailed analysis of the meridional pattern, testing the biases of sampling frequency and of the diurnal cycle, will be carried out in a later paper (M.-E. Carr et al., manuscript in preparation, 1992).

The rate of dissipation of thermal variance, χ, is shown in Figure 8*b*. The equatorial maximum seems to be somewhat more confined latitudinally. The highest individual values are observed at the equator (see Figure 15*b*) from 30 to 50 m (almost 10^{-4} °C^2 s^{-1}). Values of the order of 10^{-7} °C^2 s^{-1} are only reached in the equatorial region, and at the surface at 10°N. The general pattern is similar to that observed for dissipation. The equatorial maximum is statistically significant between 0° and 1°N at the 25 and 35 m depths; between 1°N and 1°S at 45 m, and between 0° and 1°S for 50–60 m, reflecting, as in ϵ, the larger meridional shear south of the equator (Figures 7*b* and 4*b*). The low values for 1°N below 50 m, as in dissipation, correspond to the peak in *Ri* (see Figure 7*c*).

The eddy diffusivity for mass, K_ρ, calculated using equation (7), is plotted in Figure 8*c*. This parameterization assumes that a constant fraction of the energy available for mixing is converted into buoyancy flux. The value used here for Γ is 0.25. In well-mixed layers, such as the surface layers observed around 5°N and between 5°S and 10°S, high dissipation does not imply a corresponding amount of buoyancy flux, and consequently, K_ρ overestimates the true mixing rate. Likewise, the determination of N^2 is difficult in such cases. The meridional transect shows a maximum in the equatorial region for all depth bins, although there are high values found at other latitudes as well (e.g., 10°N). Large values of N^2 are found at 0° (Figure 7*a*), which explains the displacement of the maximum to 1°S at 15 and 25 m.

The confidence intervals indicate that the equatorial maximum is statistically distinct from the values found to the south only at 15 and 65 m. The near-equatorial region to the north (1°N–2°N) presents a significant minimum with respect to the equatorial high at all depths, and corresponds to high N^2 (Figure 7*a*) and low ϵ values (Figure 8). The highest values observed are those of the top 30 m, where mean values greater than 10^{-4} m^2 s^{-1} are found.

4. Time Series at the Equator

Meteorological Conditions

Time series measurements were made at the equator for March 2–7, 1988. The meteorological conditions are shown in Figure 9. During the study period, air temperatures (mean of 27.4°C) were high, and the SST (mean of 26.2°C) were lower than usual for March. The fact that the air is warmer than the SST throughout the entire period, even at night, implies low latent heat losses and sensible heat flux into the ocean, thus decreasing the probability of convective overturning. An interesting feature is the drop in SST at year day 64 (see also Figure 10). This is the surface signature of large changes in the oceanographic conditions. The drop in SST coincides with a minimum in wind speed and with slightly decreased air temperatures during the day. The winds were low, 5.5 m s^{-1}, in agreement with long-term averages for 0° [*Moum et al.*, 1989]. The proximity to the spring equinox explains the large incoming irradiance value

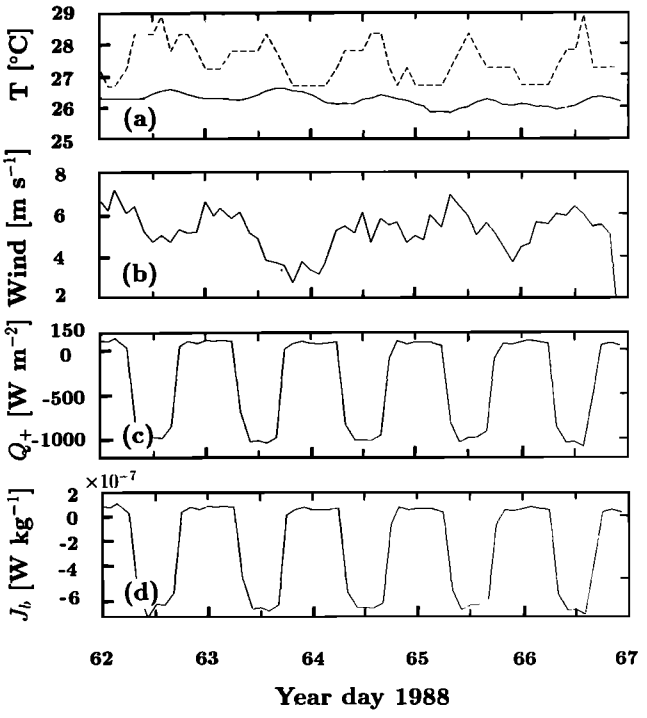

Fig. 9. Meteorological conditions at the equator. (*a*) Air (dashed line) and sea surface temperature (solid line), (*b*) wind speed, (*c*) total surface heat flux, calculated as the sum of short-wave, sensible, latent, and long-wave fluxes (a negative flux is heat into the ocean), and (*d*) buoyancy flux.

(with maxima at noon of 1000 W m^{-2}). The surface heat losses are never greater than 150 W m^{-2}, and they decrease gradually during the study period to values of 100 W m^{-2} as the SST decreases. The buoyancy flux is strongly negative during the day (heat going into the ocean) and is positive at night with maximum values of 10^{-7} W kg^{-1}. The observed nocturnal heat loss and buoyancy flux are markedly less than the Tropic Heat values (150–200 W m^{-2} and 2 × 10^{-7} W kg^{-1}).

Hydrographic Patterns

The temperature evolution of the equatorial surface layer is shown in Figure 10. The temperature at 3 m cools approximately 0.6°C between year day 63 and 65. Progressive thermal stratification of the top 20 m after day 64 is also quite clear. The diurnal signal between 5 and 10 m goes from approximate values of 0.3°C on day 63 to 0.45°C on day 64. This stratification persists throughout the night. Interestingly, as the temperature drops, the water column is stratifying. If the cooling were the result of surface forcing, it would be accompanied by convection (diminished stratification). The temperature contour plot (Figure 11*a*) also shows the cooling trend after day 64, as surface temperatures cool to values previously found around 35 m. Below 50 m there is no apparent cooling parallel to that observed at the surface except after day 65 at and below 100 m. The separation of the 16°C and 18°C isotherms coincides with intensification of the EUC on day 67 (Figure 12*a*). The salinity (Figure 11*b*) of the upper 50 m increases from less than 35.1 on day 64 to 35.25 psu late in day 66. Vertically, there is a salinity maximum centered at 60 m at the start

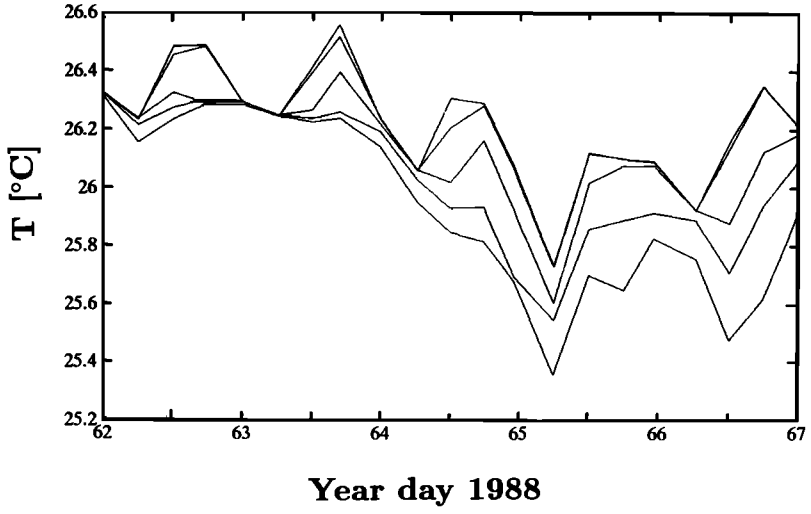

Fig. 10. Temperature in the upper layer at the equator. The lines mark the time evolution at 3-, 5-, 10-, 15-, and 20-m depths.

of the time series, which is gradually smoothed, and by day 66 the salinity of the top 70 m is uniform and of the same value found originally at the maximum.

The contour plot of relative east-west velocity (Figure 12*a*) shows intensification of the EUC starting on day 63, reaching a maximum during day 64 and another in the morning of day 67. The meridional velocity (Figure 12*b*) below 40 m changes abruptly from weak southward to northward flow early in year day 64, coinciding with the increase in salinity in the same depth range.

Nutrient and chlorophyll concentrations (Figures 12*a* and 13*c*) increase together at the surface after day 64, implying that the surface chlorophyll increase does not reflect growth in response to the enhanced nutrients, but that chlorophyll is acting as a passive tracer of the water motion. Nitrate goes from 4–5 to 6 μmol L^{-1}; chlorophyll becomes greater

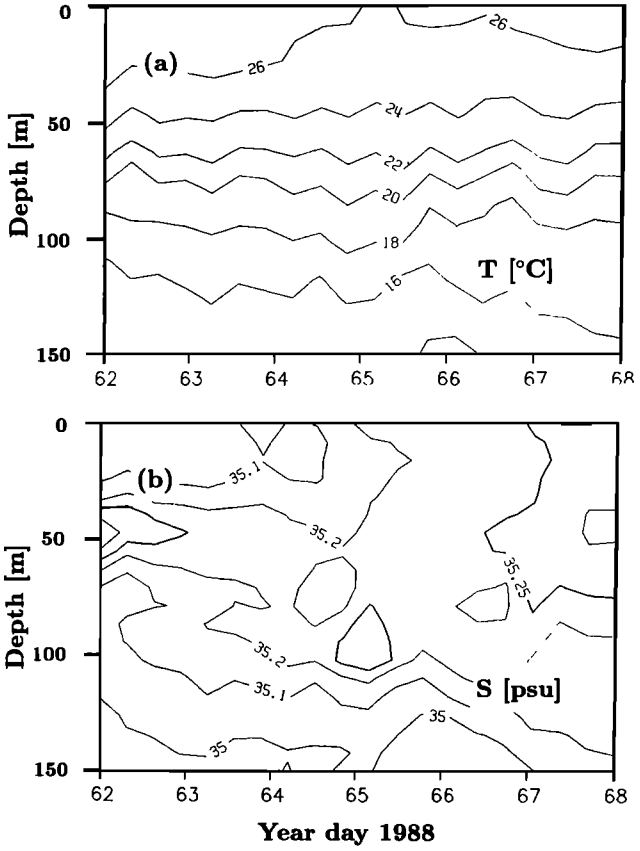

Fig. 11. Contour plots of (*a*) temperature and (*b*) salinity for the time series at the equator.

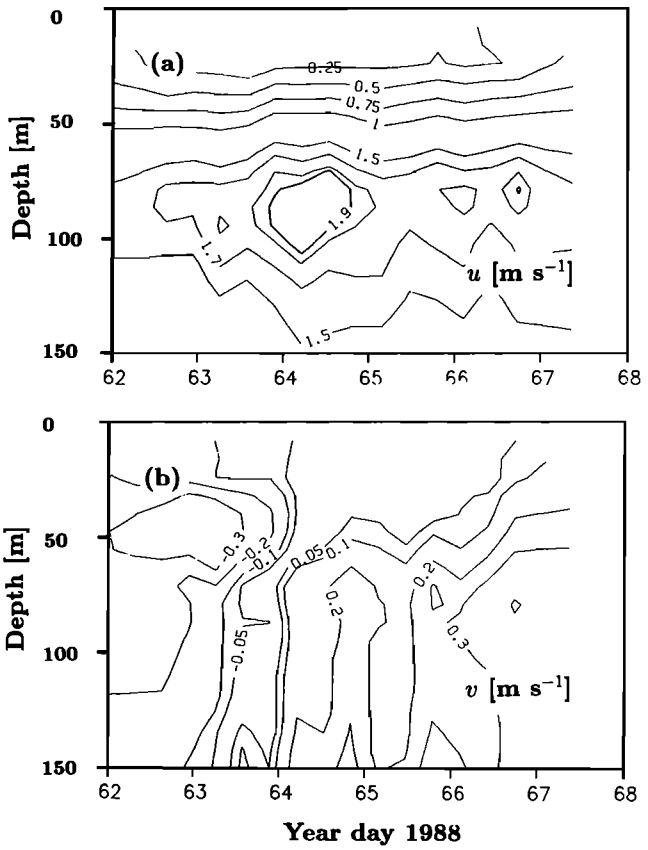

Fig. 12. Contour plots of (*a*) east-west velocity and (*b*) north-south velocity for the time series at the equator.

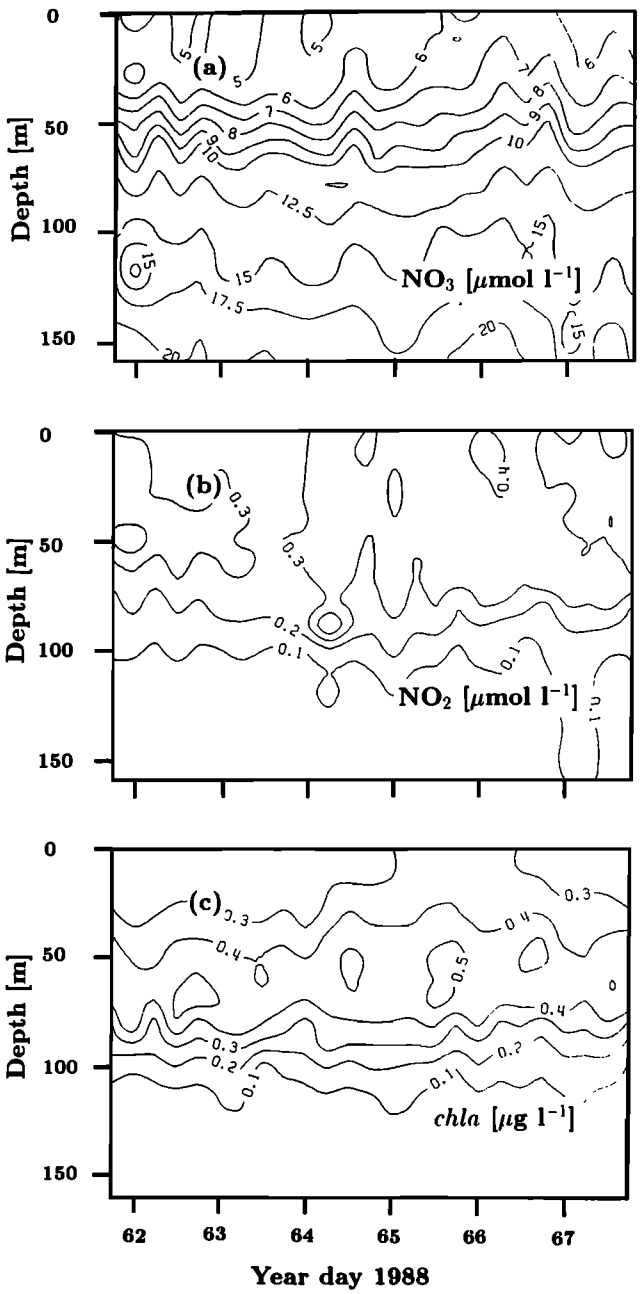

Fig. 13. Contour plots of (*a*) nitrate concentration, (*b*) nitrite concentration, and (*c*) chlorophyll concentration at the equator.

than 0.3 μg L^{-1}. Nitrite (Figure 13*b*) increases from values ranging from 0.2–0.3 μmol L^{-1} to 0.3–0.45 μmol L^{-1} after day 64 in the upper 60 m.

The change in meridional velocity is consistent with the arrival of high-salinity water from the thermocline south of the equator. The increased nitrite concentrations (Figure 13*b*) (> 0.30 μmol L^{-1}) confirm that the water comes from south of the equator, as these values were not present at any depth at 0° prior to day 64, or to the north (see Figure 5*d* for meridional transect). It seems that the EUC was not centered at the equator when we arrived, and as a result of the northward velocity, the zonal current system returned to 0° in the morning of year day 64. This would explain the intensification of the EUC at that time. The presence of cold, saltier, higher nutrient water at the surface seems to indicate upwelling.

The diurnal cycle in temperature is clearly visible in the surface layer (see also Figure 10). There is no apparent diurnal signal in salinity. Nitrate concentrations peak in the mixed layer during the late afternoon-night (see 5 and 6 μmol L^{-1} isolines in Figure 13*a*). The chlorophyll time series shows a diurnal maximum (see the 0.3 and the shallow 0.4 μg L^{-1} isolines in Figure 13*c*) at around 1800 hours, the signal of production during the day. This peak is no longer visible by morning, indicating close coupling between production and loss processes (presumably grazing or mixing). The diurnal cycle in chlorophyll standing stock and primary production is given by *Cullen et al.* [this issue]. The diurnal signals of nitrate and chlorophyll (both increasing in the afternoon) indicate that the variability in NO_3 concentration is relatively uncoupled from the phytoplankton growth. A daily change of 0.2 to 0.3 μg L^{-1} of chlorophyll is likely to result in an uptake of 0.2 to 0.3 μmol L^{-1} of inorganic nitrogen per day. The observations confirm that the nitrate concentrations are not limiting for phytoplankton growth.

The time series of N^2, U_z^2, and Ri (Figure 14) show that the variability in Ri is largely determined by N^2. Superimposed on the clear diurnal cycle of N^2 at 15 m is an increase after day 64, reflecting the growing stratification

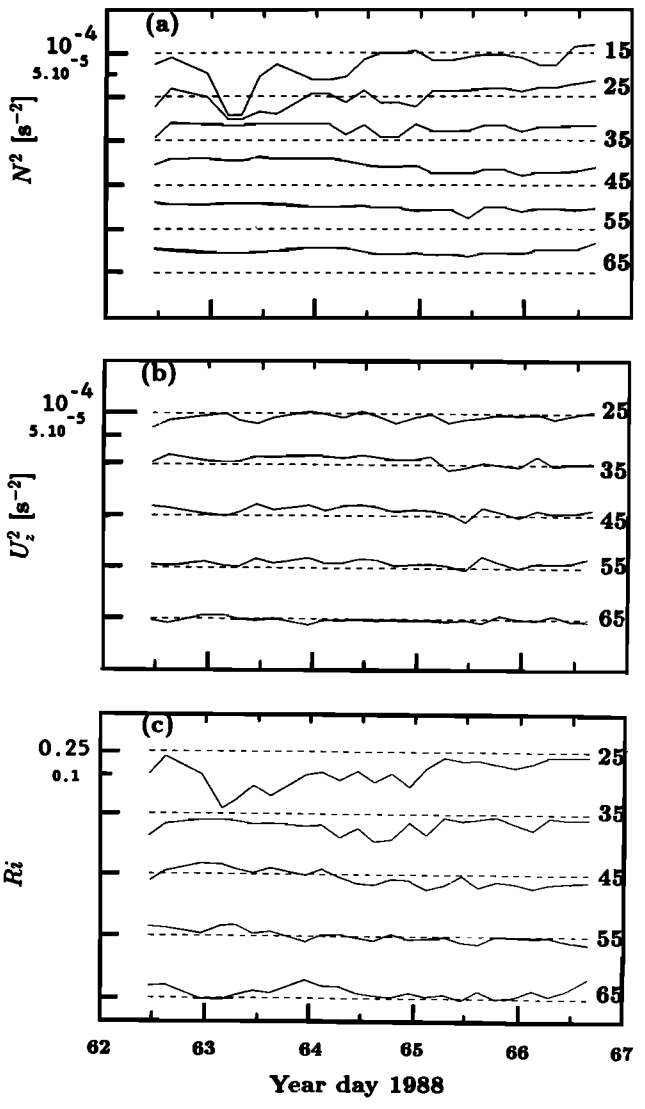

Fig. 14. Time series of (*a*) N^2, (*b*) U_z^2, and (*c*) Ri at the equator.

(Figure 10). This increase is also observable at 25 m. Concurrently, N^2 decreases at depth (especially evident at 45 m). The structure of the water column has changed by day 64.5: the well-mixed layer has been replaced by the upper pycnocline, while the sharp gradient found at intermediate depths (40–70 m) at the start of the time series has become more gradually sloped. The largest shear is found between 40 and 60 m and is quite homogeneous in that region (4×10^{-3} s^{-2}). Below the core of the EUC the shears are also large, but ELITESONDE was not able to penetrate to that depth, so they have not been plotted here. The relative minimum on day 65 corresponds to the weakening of both the EUC and the meridional flow at that time (Figure 12). *Ri* is below 1/4 after day 64 from 40 to 60 m and above 40 m (low N^2) throughout the time series.

Small-Scale Physics: Dissipation and Vertical Mixing

The time series of ϵ and χ are plotted in Figures 15*a* and 15*b*. The 95% confidence intervals of the mean value for the stations were calculated assuming a lognormal distribution [*Baker and Gibson*, 1987], and representative values are shown. The clear diurnal signal reported by other authors [*Gregg et al.*, 1985; *Moum et al.*, 1989], with high values of ϵ occurring at night and to great depth (100 m) and low values during the day as turbulent motion is suppressed by stratification, is not apparent here. The atmospheric conditions of our study period (low wind speed, high incoming irradiance, and low sea-surface temperatures) differ notably from those of Tropic Heat, where wind speeds were high (mean of 9 m s^{-1}) and the air sea temperature difference was reversed at night [*Moum et al.*, 1989], leading to large surface heat losses (150–200 W m^{-2}). Deep night-time convection, accompanied by large rates of dissipation throughout large parts of the water column [*Lombardo and Gregg*, 1989], is not as likely to occur during our study period. Likewise, at low wind speeds, the downward propagation of heat absorbed at the surface is impeded, thus limiting the vertical extent of a strongly stratified diurnal layer [*Hebert et al.*, 1991]. Another consequence of sampling in spring is the depth of the EUC. The EUC core was found at 78 m, much shallower than in the Tropic Heat measurements (125 m at 140°W) [*Peters et al.*, 1988; *Moum et al.*, 1989]. This means that the associated region of high stratification is much closer to the surface, and surface-driven mixing will be inhibited by stability at shallow depths.

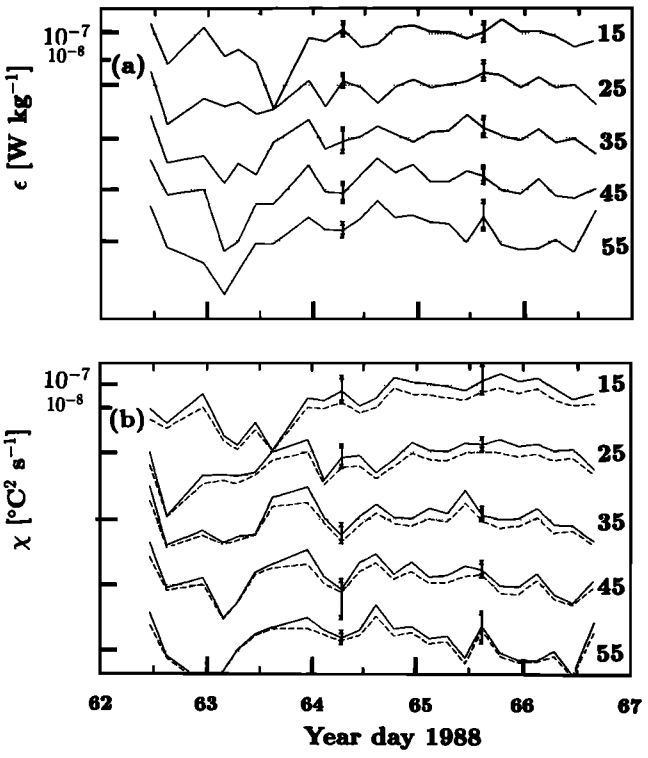

Fig. 15. Time series (*a*) of turbulent kinetic energy dissipation ϵ and (*b*) of dissipation of thermal variance χ at the equator. The dashed line in Figure 15*b* is the measured thermal variance, and the solid line is the corrected value. The 95% confidence intervals for the stations have been calculated assuming a lognormal distribution, and representative values are depicted.

In both ϵ and χ the 15-m depth interval seems to be independent of the general features observed from 20 to 60 m, which seem to be coupled. The 15-m depth interval shows some semblance of diurnal cycling, with maximum values occurring during the night or late in the day and minima around noon. There is a conspicuous minimum on year day 63 in both ϵ and χ. This minimum coincides with a peak in N^2 following the extreme low in the early hours of day 63 as well as with a sharp drop in wind speed. After year day 63.5 the values for ϵ and χ become larger. This increase occurs first at depth and then moves toward the surface within few hours. The largest increase is observed at 55 m (as well as the largest values of ϵ and χ), and it becomes smaller as it progresses upward. The increase is very small or nonexistent at 25 m, although it is quite noticeable in the surface bin. The steady increase in ϵ and χ corresponds to decreasing *Ri* (to close to 1/4) below 30 m after day 64 and with an increase of the already critical values at 25 m at the same time (Figure 14*c*). Insufficient information about the upper 20 m makes it difficult to reach any conclusion at this stage as to whether the 15-m bin is coupled to the deeper forcing or whether it is independent.

The observation of high ϵ and χ values at depth preceding the ones in shallower water is consistent with the "arrival" of the EUC to the sampling site. Intense zonal velocities and upwelling modify the structure of the water column, converting the entirety of the sampled region into a gradually sloping thermocline.

The eddy diffusivity coefficients are given in Figure 16. The 15-m depth interval exhibits a diurnal cycle in all three coefficients. Below 30 m, the patterns for the remaining depth bins are similar and seemingly independent of the surface forcing. The major features seem to first appear at depth, as was observed for χ and ϵ. The increase after year day 63 is noticeable for the 35, 45, and 55 m bins but not for the two surface bins. The three coefficients present a similar pattern, especially K_ρ and K_m below 30 m. The largest values are observed in the 15-m depth interval (K_T and K_ρ) and from 40 to 60 m. K_T values were generally larger than K_ρ, especially at the surface. In the *Peters et al.* [1988] study, K_ρ was approximately 3 times the value of K_T.

A value for Γ was obtained by comparing the temperature variance and ϵ and assuming that K_T and K_ρ should be the same. The mean Γ for the equatorial time series from 10 to 60 m was 0.399 (the 95% confidence intervals of the lognormal distribution are given by $0.062 < 0.399 < 1.376$). This is somewhat larger than the value usually cited but is

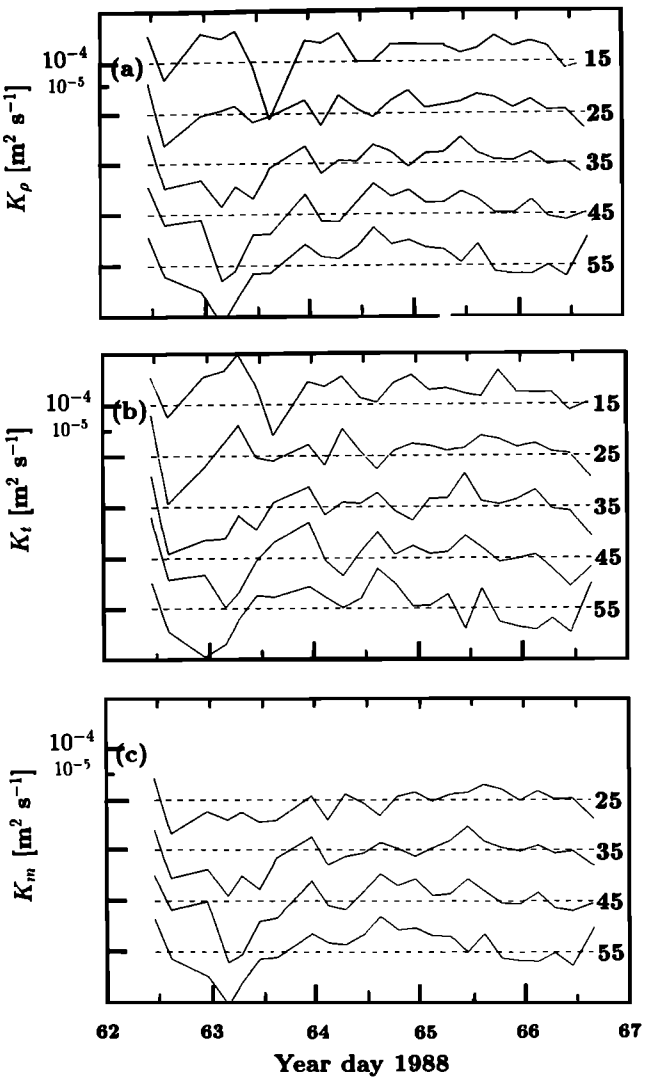

Fig. 16. Time series of the vertical eddy diffusivity coefficient for (*a*) mass K_ρ, (*b*) heat K_T, and (*c*) momentum K_m at the equator.

within the 95% confidence intervals for the distribution calculated by *Oakey* [1985]. The fact that it is larger than the value of 0.1 obtained in Tropic Heat [*Peters et al.*, 1988] reflects the relative values of K_T and K_ρ and is a consequence of the thermal stratification observed in the upper part of the water column. Γ depends on Ri [*Rohr and Van Atta*, 1987], being low at very small Ri (well-mixed layers, low N^2) then increasing to $Ri \simeq 1/4$, and falling thereafter as increased stability impedes mixing. The smallest Γ values (mean for the profile, 0.09) were observed coinciding with the extreme N^2 and Ri minimum near the end of year day 62 (Figure 14). The relationship between Γ and Ri and between the different diffusivity coefficients will be dealt with in detail in a later paper (M.-E. Carr et al., manuscript in preparation, 1992).

The turbulent vertical heat flux is portrayed in Figure 17. There is a diurnal cycle in the top bin, but it is obscured by large fluxes in the daytime on days 62 and 63. The mixed layer is never deeper than 25 m, so the top bin represents the loss of heat to the mixed layer. The mean heat flux from the surface layer (around 40 W m^{-2}) is comparable in size

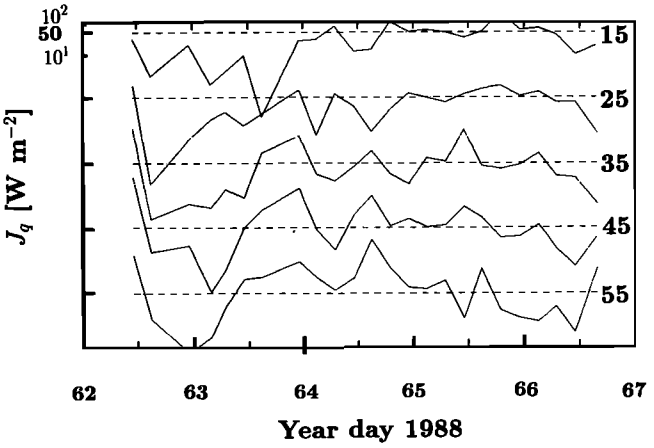

Fig. 17. Time series of heat flux J_q at the equator.

to the penetrative irradiance at that depth [*Carr and Lewis*, 1990] and to the surface latent heat loss. The increasing trend after day 64 is a consequence of the increasing thermal stratification from 10 to 20 m rather than of enhanced mixing. The 25-m depth bin also responds to the increased temperature gradient, and the downward flux is rarely of O(50 W m^{-2}). It is below 30 m that the heat flux is largest. At these depths, temporal variability is determined by the K_T patterns, not the gradients (which decrease). On day 64, extraordinarily large heat fluxes are observed from 40 to 60 m, ranging from 500 to 1000 W m^{-2} in response to K_T values of 10^{-3} m^2 s^{-1}. This vertical structure is in contrast to the Tropic Heat results, where maximum heat flux values were observed in the top 30 m (mixed layer) [*Moum et al.*, 1989].

5. Parameterization of Mixing

One of the goals of experiments such as Tropic Heat [*Eriksen*, 1985] has been to find a parameterization of mixing for the equatorial region using large-scale variables that are more easily obtained. Comparison has been made throughout our study between the large-scale measurements made with the CTD and ADCP, which are gathered routinely on ships, and the microscale measurements. An estimate of mixing is obtained when we merge the microstructure parameters, ϵ and χ, with the large-scale observations such as the temperature gradient (for K_T), N^2 (for K_ρ), and the velocity gradient (for K_m). We have used the variability in Ri to understand the meridional and temporal patterns of ϵ and χ as it determines the regions that are susceptible to turbulent mixing.

Modelling of equatorial dynamics has received new impetus as the global consequences of the interannual variability (ENSO) become increasingly evident. As in all circulation models, there is an ongoing debate about a proper choice for diffusivity parameterization. Since the equatorial region is characterized by high stratification and a large mean steady shear, attempts have been made to find a parameterization based on the Richardson number [*Pacanowski and Philander*, 1981] (hereafter PP). This is not straightforward because the Ri provides a threshold criterion for turbulent mixing and there is not necessarily any proportionality between the value of Ri and the intensity of the mixing, which will depend instead on the forcing terms. In the PP scheme $K(Ri)$ increases gradually as Ri becomes smaller.

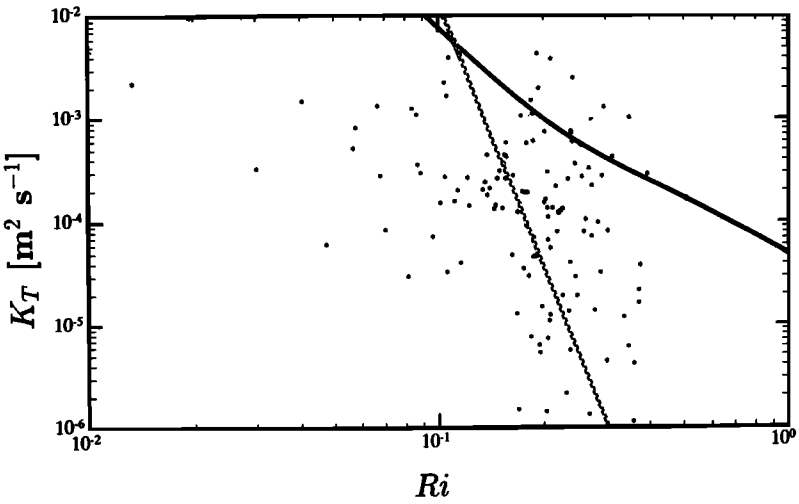

Fig. 18. The eddy diffusivity coefficient of heat K_T as a function of the Richardson number Ri. The dashed line is the linear least squares power law that fits the data and the solid line is the parameterization of *Pacanowski and Philander* [1981].

Comparison with actual data [*Peters et al.*, 1988] indicates that this scheme is not appropriate for the low Ri found in the high shear zone of the EUC, where the mixing coefficient increased much more than predicted. They suggested a parameterization with two separate expressions, a power function for the high shear zone and a second fit, with a functional form similar to that of PP, for the high Ri values found in the core of the undercurrent.

Another approach was given by *Moum et al.* [1989]. They found that the distribution of Ri versus ϵ also suggested a two-state process, with two distinct "populations" of ϵ for small and large Ri. They concluded that ϵ could not be predicted from Ri and proposed instead a cutoff value of $Ri = 0.7$, which represents a boundary between the two regimes. If the measured Ri value falls above or below the cutoff, a mean ϵ would be assigned accordingly from the population of each regime.

Our data are more limited than that of Tropic Heat [*Peters et al.*, 1988; *Moum et al.*, 1989], as we were not able to penetrate the core of the EUC and therefore we do not have any data with high Ri. The effects of night-time convection did not penetrate below 20 m, so the Ri link to ϵ is not obscured by diurnal cycling. K_m and K_T are portrayed as a function of Ri in Figure 18. The gradually sloping PP parameterization obviously does not apply to our observations, which resemble those of *Peters et al.* [1988] and *Moum et al.* [1989] for the high shear zone over the EUC. We carried out a linear least squares fit of the diffusivity coefficient K_T to a power law of Ri and obtained

$$K_T = 3.91 \times 10^{-11}\, Ri^{-8.48\pm40} \qquad [\mathrm{m^2\ s^{-1}}] \quad (12)$$

Although diffusivity decreases with increasing Ri, the scatter is considerable. This degree of uncertainty is not surprising, since the highest dissipation values were found at depth, while the lowest Ri were those of the upper 40 m (Figures 14 and 15). Our results confirm a lack of correlation between Ri and mixing intensity once critical values are approached.

In a recent paper by *Schudlich and Price* [1991] the equatorial diurnal cycle is modelled using the forcing measured during Tropic Heat and a diurnal upper ocean model. Mixing occurs due to shear flow instability such that the Richardson number does not fall below 1/4. Dissipation is estimated using the flux and shear profiles. Although the overall value of ϵ, as well as the intermittent nature of dissipation are well simulated in the model, there is no correlation of the time series distribution to either the observations or to the surface forcing. This is attributed to the presence of internal waves as triggers initiating instabilities in the real ocean.

6. Discussion

The WEC88 cruise surveyed from 15°N to 15°S with a 6-day time series at the equator. The observed hydrographic patterns along the transect are comparable to those observed by *Wyrtki and Kilonsky* [1984]. Temperature and nutrient concentrations show the typical equatorial doming. The salinity front separating low-salinity water to the north and high-salinity water to the south is clearly visualized by the 35 psu isoline. The relative east-west velocity indicated the core of the EUC was located at 78 m, a typical depth for the spring period. Meridional flow was divergent above the core of the EUC and converged at and below 80 m. This classical circulation cell is thought to be a consequence of the change in flow direction during the time series. Presumably, the sign change obscured the high-frequency variability when averaging.

The meridional transect was used to address the issue of the existence of an equatorial maximum in turbulent dissipation. A composite data set prior to Tropic Heat [*Crawford*, 1982] revealed a strong maximum in energy dissipation, ϵ, within 100 km of the equator. Subsequent studies have not always found a dissipation maximum so narrowly confined to the equator. Intensive sampling in the Tropic Heat program revealed that at the equator itself, temporal variability associated with the diurnal cycle [*Gregg et al.*, 1985] was very large (100-fold) and that there was a strong relationship between turbulent mixing in the upper layer and local winds [*Moum et al.*, 1986, 1989]. Dissipation was found to be higher than predicted by scaling with the surface buoyancy flux [*Moum et al.*, 1989], and the excess was attributed to shear production [*Peters et al.*, 1989]. *Moum et al.* [1989] reported that for a transect from 3°N to 3°S there was no

spatial variation in ϵ associated with either the equator or the EUC. A recent study [*Peters et al.*, 1989] distinguished between the dissipation in the thermocline and that of the mixed layer and found that dissipation in the thermocline peaked within a degree of the equator. The existence of an equatorial maximum in dissipation is still being debated.

The meridional patterns of the dissipation of turbulent kinetic energy ϵ, and of thermal variance χ, were examined here by comparing the values at each depth bin along the transect. Because mixed layer depth changes considerably with latitude, this approach implies comparison between mixed layer and thermocline values. *Peters et al.* [1989] integrated ϵ with depth and separated the mixed layer and thermocline values. His observation of a maximum in thermocline dissipation at 0° is consistent with our result of a larger peak at depth. We have chosen to compare each depth bin rather than integrated or averaged values, so as to better distinguish the vertical structure of the mixing regime at each site. Thus we can see that the high values observed at 10°N are confined to the upper part of the water column, as corresponds to direct surface forcing, and that the high ϵ and χ measurements at 0° extend throughout the top 60 m. In fact, the deeper levels lead those closer to the surface. The averaged or integrated values of ϵ or χ over the top 70 m reveal the same characteristic peak. Although 70 m was the lowest depth sampled at the equator, off-equatorial dissipation values below that depth were less than 10^{-8} W kg^{-1}.

Most studies of the equatorial region, including this one, have concentrated sampling at 0°, and the "mean" values used to illustrate the meridional structure are obscured by the sampling intensity at each latitude. This can be improved somewhat by attempting to cover the diurnal cycle at each site and by estimating the bias associated with the time and intensity of sampling [*Peters et al.*, 1989]. In our study we tried to sample the diurnal cycle at all latitudes, although our sampling frequency is much below that of the Tropic Heat studies. Our results indicate that there is statistically significant spatial variability associated with the equatorial region. This is related to the presence of the EUC as well as to the meridional flow patterns, which can be decisive in bringing the Ri to critical values.

The time series at the equator was characterized by a decrease in SST and increase in salinity on year day 64. This coincides with a shift from southward to northward velocities below 50-m depth and intensification of the EUC. It is proposed that the EUC was centered south of 0° when we commenced the time series. We then sampled an abrupt change from south to northward velocity, which returned the zonal current system to the equator. The presence of high nitrite concentrations after day 64 reinforces the hypothesized off-equatorial origin, as opposed to the explanation that the colder, saltier surface water is a consequence solely of upwelling. The changes in surface water characteristics, e.g., decreased temperature and increased salinity and nutrient concentrations as well as increased N^2 of the top 30 m, indicate enhanced upwelling in addition to increased mixing rates. It is possible that we sampled the shift from the southward to northward phase of a 20-day oscillation, but longer velocity time series or satellite images of SST during that period would be necessary to corroborate this option.

The small-scale physics likewise reflects the changing regime, and there is an increase in both ϵ and χ following day 63. The temporal patterns below 20 or 30 m are closely related and preceded by those at 55 m. The surface patterns seem to be independent and to respond instead to surface forcing. There is no diurnal signal below 25 m. The three eddy diffusivity coefficients give similar results. The surface and 25-m depth interval present a diurnal cycle and do not show an increase after year day 63. The patterns at depth seem to be related. The increase observed after year day 63 for ϵ and χ is seen for the 45- and 55-m depth bins. The values of ϵ, χ and all three diffusivity coefficients are greatest at the 55-m depth interval, rather than at 65 m. This reflects the reduced shear in the 60–70 m depth range immediately preceding the sharpest velocity increase approaching the EUC core.

The role of small-scale processes in the large-scale dynamics of the equatorial region is still not clear. In the absence of Coriolis force at 0°, turbulent stress divergence has been proposed as a significant term in the energy balance of the zonal current system [*Crawford*, 1982; *Gregg et al.*, 1985; *Bryden and Brady*, 1989]. Recent measurements seem to indicate, however, that this term is smaller than necessary to balance the zonal wind stress [*Dillon et al.*, 1989]. The vertical turbulent heat flux together with surface fluxes, advection and penetrative irradiance determine the temperature of the pool of cold water that extends westward from South America [*Eriksen*, 1985; *Gregg et al.*, 1985; *Carr and Lewis*, 1990; *Lewis et al.*, 1990]. *Gregg et al.* [1985] and *Moum et al.* [1989] found that the turbulent vertical heat flux plus the irradiance penetrating the upper 20 m was almost equal to the total surface heat flux.

In our observations, the vertical heat flux out of the surface layer was the same order of magnitude as the penetrative irradiance $O(40\ \mathrm{Wm^{-2}})$, and both were significantly smaller than the total surface heat flux. The time series of turbulent heat flux revealed the same pattern as ϵ and χ: a weak diurnal signal in the upper 20 m and maximum values, $O(500\ \mathrm{W\ m^{-2}})$, at 55 m, corresponding to the large K_T and T_z values.

Our observations differ notably from those of Tropic Heat, where the largest dissipation rates were observed at the surface; in our study, maximum values of ϵ, χ, and heat flux occur at depth. The major features seem to then move upward within few hours. Likewise, a major result of their study was the extreme diurnal cycle that reached great depth. In our study, the diurnal cycle was limited to the top bin (10–20 m). An explanation can be found in the less vigorous surface forcing during our study period as well as the significantly shallower EUC core, which led to large stratification close to the surface, thus impeding convective surface-driven mixing. A modelling study [*Schudlich and Price*, 1991] that studied the sensitivity of the diurnal cycle to various factors found that if the core of the EUC was shallower, the night-time mixing would not penetrate below the core. This is consistent with our observations and confirms the role of the EUC depth in controlling the extent of nocturnal mixing.

Ri was extremely useful in predicting the spatial pattern of mixing when comparison was made between large and small values along the meridional transect. However, in the equatorial time series, where all Ri were less than 0.45 (because of the limited depth range sampled) the lowest values did not correspond to higher dissipation rates. This is consistent with a lack of proportionality between Ri and mixing intensity in the vicinity of critical Ri.

A close look at $K(Ri)$ for the upper equatorial layer re-

vealed that the PP parameterization [*Pacanowski and Philander*, 1981] does not describe our observations of mixing. A fit to a power law similar to that of *Peters et al.* [1988] describes the data, but the error bars are very large. This is not surprising, since Ri is only a threshold criterion for the occurrence of turbulent mixing. Our results show that once close to critical Ri values, mixing intensity is not proportional to the value of Ri, lending support to the *Moum et al.* [1989] scheme of a cutoff Ri to obtain an estimate of mixing given large-scale measurements or model output.

7. Conclusions

1. The observed large-scale patterns of temperature, salinity, nutrients, and chlorophyll were typical for the central equatorial Pacific. The current structure corresponded to the classical circulation cell. The EUC was centered at 78 m, a typical depth for boreal spring.

2. There was a maximum in ϵ and χ in the equatorial region at all depths.

3. The Ri, estimated using measurements made with the CTD and ADCP, was useful in predicting the regions susceptible to turbulent mixing for the meridional transect.

4. In the equatorial time series, a change from southward to northward velocity was observed on year day 64. This was followed by intensification of the EUC. It is proposed that the change in meridional velocity returned the EUC to 0°.

5. The return of the EUC to the equator coincided with lower temperatures, and higher stratification, salinity, nutrient, and chlorophyll concentrations in the upper water column. Likewise, ϵ, χ, and vertical diffusivity values increased at that point.

6. The diurnal cycle of ϵ and χ was limited to the top 20 m and was not very pronounced. Maximum values of ϵ and χ were observed at depth (55 m) in the high shear zone above the EUC core. The three vertical diffusivity coefficients calculated, for heat (K_T), mass (K_ρ), and momentum (K_m), revealed a stronger diurnal cycle but also limited to the upper 30 m.

7. Turbulent heat flux was maximum at depth, corresponding to high K_T and temperature gradients. The turbulent heat flux at the base of the surface layer was of the same order of magnitude as the penetrative irradiance, and both were much smaller than the surface heat flux.

8. For the equatorial time series, Ri was not a good predictor of mixing. All Ri were lower than 0.45, as we were not able to sample the high Ri region of the EUC core. The lowest Ri were observed at the surface (lowest N^2), while the largest ϵ and mixing coefficients were found at depth. Our estimates of equatorial mixing are better parameterized by a threshold criterion than by a power law.

Acknowledgments. We thank Scott McLean, Rob Palmer, and Dave Hazen for data collection; Dave Hazen for processing the ADCP data; and Dan Kelley and Barry Ruddick for many comments on an earlier version. Owen Hertzman, Glen Lesins, and Chris Garrett assisted in discussions concerning several parts of the work. We are also indebted to two anonymous reviewers, who provided several helpful suggestions. This work was supported by the National Science and Engineering Research Council, Strategic Grant Program (Canada).

References

Baker, M. A. and C. H. Gibson, Sampling turbulence in the stratified ocean: Statistical consequences of strong intermittency, *J. Phys. Oceanogr., 17,* 1817–1836, 1987.

Bjerknes, J., Atmospheric teleconnections from the equatorial Pacific, *Mon. Weather Rev., 97,* 163–172, 1969.

Brady, E. C. and H. L. Bryden, Estimating vertical velocity at the equator, *Oceanol. Acta (Proceedings International Symposium on Equatorial Vertical Motion),* 33–37, 1987.

Bryden, H. L. and E. C. Brady, Diagnostic model of the three-dimensional circulation in the upper equatorial Pacific ocean, *J. Phys. Oceanogr., 15,* 1255–1273, 1985.

Bryden, H. L. and E. C. Brady, Eddy momentum and heat fluxes and their effects on the circulation of the equatorial Pacific, *J. Mar. Res., 47,* 55–79, 1989.

Carr, M.-E. and M. R. Lewis, Mixing and bio-optical influences on the diurnal variability of sea-surface temperature, *Eos Trans. AGU, 71,* 123, 1990.

Chavez, F. P., Size distribution of phytoplankton in the central and eastern tropical Pacific, *Global Biogeochem. Cycles, 3,* 27–35, 1989.

Chavez, F. P. and R. T. Barber, An estimate of new production in the equatorial Pacific, *Deep Sea Res., 34,* 1229–1243, 1987.

Chereskin, T. K., J. N. Moum, P. J. Stabeneo, D. R. Caldwell, C. A. Paulson, L. A. Regier, and D. Halpern, Fine-scale variability at 140°W in the equatorial Pacific, *J. Geophys. Res., 91,* 12,887–12,898, 1986.

Crawford, W. R., Pacific equatorial turbulence, *J. Phys. Oceanogr., 12,* 1137–1149, 1982.

Cullen, J. J., M. R. Lewis, C. O. Davis, and R. T. Barber, Photosynthetic characteristics and estimated growth rates indicate grazing is the proximate control of primary production in the equatorial Pacific, *J. Geophys. Res.,* this issue.

Dillon, T. M., J. N. Moum, T. K. Chereskin and D. R. Caldwell, Zonal momentum balance at the equator, *J. Phys. Oceanogr., 19,* 561–570, 1989.

Efron, B. and G. Gong, A leisurely look at the bootstrap, the jackknife, and cross-validation, *Am. Statist., 37,* 36–48, 1983.

Eriksen, C. C., The Tropic Heat Program: An overview, *Eos Trans. AGU, 66,* 50–52, 1985.

Gill, A. E., *Atmosphere-Ocean Dynamics,* 662 pp, Academic, San Diego, Calif., 1982.

Gregg, M. C., H. Peters, J. C. Wesson, N. S. Oakey, and T. J. Shay, Intensive measurements of turbulence and shear in the equatorial undercurrent, *Nature, 318,* 140–144, 1985.

Halpern, D. and P. H. Freitag, Vertical motion in the upper ocean of the equatorial eastern Pacific, *Oceanol. Acta (Proceedings International Symposium on Equatorial Vertical Motion),* 19–26, 1987.

Halpern, D., R. A. Knox, D. S. Luthier, and S. G. H. Philander, Estimates of equatorial upwelling between 140° and 110°W during 1984, *J. Geophys. Res., 94,* 8018–8020, 1989.

Hebert, D. L., J. N. Moum, C. A. Paulson, D. R. Caldwell, T. K. Chereskin, and M. J. McPhaden, Detailed structure of the upper ocean in the central equatorial Pacific during April 1987, *J. Geophys. Res., 96,* 7127–7136, 1991.

Horel, J. D. and J. M. Wallace, Planetary-scale atmospheric phenomena associated with the Southern Oscillation, *Mon. Weather Rev., 109,* 813–829, 1981.

Janowiak, J. E., The global climate for March-May 1988: the end of the 1986–1987 Pacific Warm Episode and the onset of widespread drought in the United States, *J. Clim., 1,* 1019–1042, 1988.

Lewis, M. R., M.-E. Carr, G. Feldman, W. Esaias, and C. McClain, Satellite estimates of the influence of penetrating solar radiation on the heat budget of the equatorial Pacific ocean, *Nature, 347,* 543–545, 1990.

Lombardo, C. P. and M. C. Gregg, Similarity scaling of viscous and thermal dissipation in a convecting surface boundary layer, *J. Geophys. Res., 94,* 6273–6284, 1989.

McPhaden, M. J. and B. A. Taft, Dynamics of seasonal and intraseasonal variability in the eastern equatorial Pacific, *J. Phys. Oceanogr., 18,* 1713–1732, 1988.

Miles, J. W., On the stability of heterogeneous shear flows, *J. Fluid Mech., 10,* 496–508, 1961.

Moum, J. N., C. A. Paulson, T. K. Chereskin, and L. A. Regier, Does oceanic turbulence peak at the equator?, *J. Phys. Oceanogr., 16,* 1991–1994, 1986.

Moum, J. N., D. R. Caldwell, and C. A. Paulson, Mixing in the equatorial surface layer and thermocline, *J. Geophys. Res., 94,* 2005–2021, 1989.

Oakey, N. S., Statistics of mixing parameters in the upper ocean

during JASIN phase 2, *J. Phys. Oceanogr., 15,* 1662–1675, 1985.

Oakey, N. S., An instrument to measure turbulence in the deep ocean, *IEEE J. Oceanic Eng., 13,* 124–128, 1988.

Osborn, T. R., Estimates of the local rate of vertical diffusion from dissipation measurements, *J. Phys. Oceanogr., 10,* 83–89, 1980.

Osborn, T. R. and C. S. Cox, Oceanic finestructure, *Geophys. Fluid Dyn., 3,* 321–345, 1972.

Osborn, T. R. and W. R. Crawford, An airfoil probe for measuring velocity fluctuations in water, in *Air-Sea Interactions: Instruments and methods,* edited by F. W. Dobson, L. Hasse and R. Davis, pp. 369–386, Plenum, New York, 1980.

Pacanowski, R. C. and S. G. H. Philander, Parameterization of vertical mixing in numerical models of the tropical Pacific, *J. Phys. Oceanogr., 11,* 143–1451, 1981.

Peña, M. A., M. R. Lewis, and W. G. Harrison, Primary productivity and size structure of phytoplankton biomass on a transect of the equator at 135°W in the Pacific ocean, *Deep Sea Res., 37,* 295–315, 1990.

Peters, H. and M. C. Gregg, Some dynamical and statistical properties of equatorial turbulence, in *Small-scale turbulence and mixing in the ocean, Oceanogr. Series 46,* edited by J. C. J. Nihoul and B. M. Jamart, pp. 185–200, Elsevier, New York, 1988.

Peters, H., M. C. Gregg, and J. M. Toole, On the parameterization of equatorial turbulence, *J. Geophys. Res., 93,* 1199–1218, 1988.

Peters, H., M. C. Gregg, and J. M. Toole, Meridional variability of turbulence through the equatorial undercurrent, *J. Geophys. Res., 94,* 18,003–18,009, 1989.

Philander, G., El Niño and La Niña, *Am. Sci., 77,* 451–459, 1989.

Rohr, J. and C. Van Atta, Mixing efficiency in stably stratified growing turbulence, *J. Geophys. Res., 92,* 5481–5488, 1987.

Schudlich, R. R. and J. F. Price, Diurnal cycles of current, temperature, and turbulent dissipation in a model of the equatorial upper ocean, *J. Geophys. Res.,* in press, 1991.

Siegel, D. A. and T. D. Dickey, On the parameterization of irradiance for open ocean photoprocesses, *J. Geophys. Res., 92,* 14,648–14,662, 1987.

Smith, S. D., Coefficients for sea-surface wind stress, heat flux, and wind profiles as a function of wind speed and temperature, *J. Geophys. Res., 93,* 15,467–15,472, 1988.

Toole, J. M., H. Peters, and M. C. Gregg, Upper ocean shear and density variability at the equator during Tropic Heat, *J. Phys. Oceanogr., 17,* 1397–1406, 1987.

Trenberth, K. E., G. W. Branstator, and P. A. Arkin, Origins of the 1988 North American Drought, *Science, 242,* 1640–1645, 1988.

Whitledge, T. E., S. C. Malloy, C. J. Patton, and C. D. Wirick, Automated nutrient analyses in seawater, 216 pp., *BNL 51398,* Brookhaven National Laboratory, Upton, N. Y., 1981.

Wilson, D. and A. Leetmaa, Acoustic Doppler current profiling in the equatorial Pacific in 1984, *J. Geophys. Res., 93,* 13,947–13,966, 1988.

Wunsch, C. and A. E. Gill, Observations of equatorially trapped waves in Pacific sea level variations, *Deep Sea Res., 23,* 371–390, 1976.

Wyrtki, K., Sea level and seasonal fluctuations of the equatorial currents in the western Pacific ocean, *J. Phys. Oceanogr., 5,* 91–103, 1974.

Wyrtki, K., El Niño - The dynamic response of the equatorial Pacific ocean to atmospheric forcing, *J. Phys. Oceanogr., 5,* 572–584, 1975*a*.

Wyrtki, K., Fluctuations of the dynamic topography in the Pacific ocean, *J. Phys. Oceanogr., 5,* 450–459, 1975*b*.

Wyrtki, K. and B. Kilonsky, Mean water and current structure during the Hawaii to Tahiti shuttle experiment, *J. Phys. Oceanogr., 14,* 242–254, 1984.

M.-E. Carr, College of Oceanography, Oceanography Administration Building 104, Oregon State University, Corvallis, OR 97331.

B. Jones, Institute of Marine Sciences, University of Southern California, Los Angeles, CA 90089.

M. R. Lewis, Department of Oceanography, Dalhousie University, Halifax, Nova Scotia, Canada B3H 4J1.

N. S. Oakey, Department of Fisheries and Oceans, Bedford Institute of Oceanography, Dartmouth, Nova Scotia, Canada B2Y 4A2.

(Received July 2, 1990;
accepted March 11, 1991.)